# Short Papers

## Antenna Arrays in MCM-D Technology Fed by Coplanar CPW Networks

Ezzeldin A. Soliman, Steven Brebels, Guy A. E. Vandenbosch, and Eric Beyne

***Abstract*—In this paper, the design, fabrication, and characterization of planar antenna arrays in the MCM-D technology are presented. The arrays are fed by coplanar feeding networks built using coplanar-waveguide lines. 2 × 2 and 4 × 4 arrays of slot dipoles designed to work in *K*-band, around 25 GHz, are also presented. The analysis was carried out both theoretically and experimentally. The results include the return loss, radiation patterns, and antenna gain. The proposed arrays are compatible with the driving electronics technology, enjoying high-impedance bandwidth, low cross polarization, high gain, and high radiation efficiency.**

***Index Terms*—Coplanar CPW networks, MCM-D technology, planar antenna arrays.**

### I. Introduction

Planar antenna arrays are interesting candidates for microwave and millimeter-wave applications, especially in mobile communications where low profile and light weight are important considerations. In order to excite the elements of the array, a feeding network must be realized. The feeding network can be either series- or parallel-fed. Several authors have given a lot of interest to the feeding network [1], [2]. Unlike microstrip antenna arrays, coplanar antenna arrays have received only little attention in the literature. A coplanar-waveguide (CPW)-based feeding network has several advantages over a microstrip feeding network, such as low radiation losses, less dispersion, easier in combining active devices with the elements to form an active array, and the possibility of connecting shunt lumped elements to the active devices without the need of via holes through the substrate. Slot-type radiators have appealing properties such as the wide impedance bandwidth, high radiation efficiency, and the possibility of obtaining bi-directional [3] and unidirectional radiation patterns [4]. The main drawback of the CPW-based feeding network is the possible excitation of the parasitic slotline mode at the location of the discontinuities. The MCM-D technology has been proven to offer a cost effective and mechanically stable way for the suppression of the parasitic modes [5]. It uses an overpass bridge over a thin film deposited over the CPW. The bridge is connected to the required locations on the CPW through via holes photo patterned in the thin film. In this paper, we will present 2 × 2 and 4 × 4 arrays of slot dipoles built in the MCM-D technology. The 2 × 2 sub-array is fed using an *H*-resonator [1], which provide a more compact design than the corporate feed. The sub-arrays are connected using a coplanar feeding network to form a 4 × 4 array. Experimental and theoretical results of the proposed antennas are presented and discussed.

Manuscript received March 2, 1999.

E. A. Soliman is with IMEC, B-3001 Leuven, Belgium, and is also with the ESAT-TELEMIC Division/Elektrotechniek Department, Katholieke Universiteit Leuven, B-3001 Leuven, Belgium.

S. Brebels, and E. Beyne are with IMEC, B-3001 Leuven, Belgium.

G. A. E. Vandenbosch is with the ESAT-TELEMIC Division/Elektrotechniek Department, Katholieke Universiteit Leuven, B-3001 Leuven, Belgium.

Publisher Item Identifier S 0018-9480(00)04673-1.

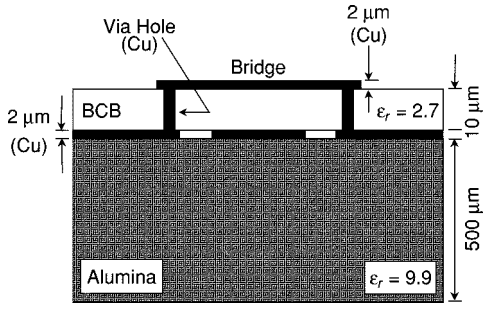


Fig. 1. Layer structure of the microwave MCM-D technology.

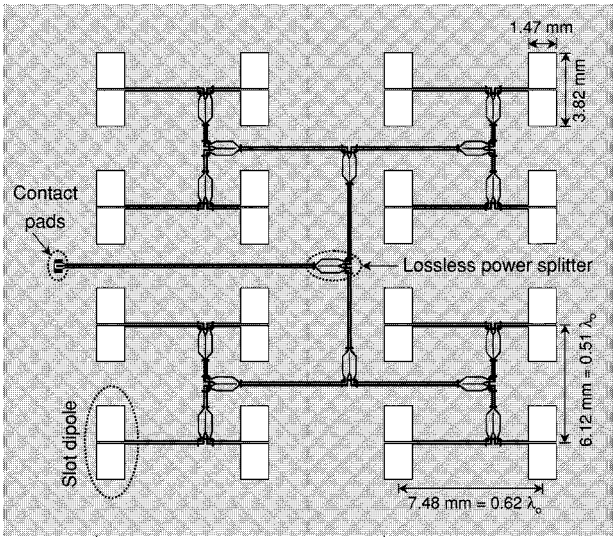


Fig. 2. Layout of the 4 × 4 array of slot dipoles fed by CPW network.

### II. Design of the Antenna Arrays

The layer structure used to realize the antenna arrays is shown in Fig. 1. The substrate used is a standard microwave substrate of Alumina, $Al_2O_3$, with $\varepsilon_r$ = 9.9 and thickness of 500 $\mu$m. A thin dielectric film of BCB, with $\varepsilon_r = 2.7$ and thickness of 10 $\mu$m, is deposited on the substrate. This thin film is a typical property of the MCM-D technology, which uses it as an insulator between two layers of interconnects running on both sides of that thin film. Connections between these two layers are possible through photo-patterned via holes in the thin film. The bottom metal layer is used to realize the CPW-based microwave circuit. At the location of the discontinuities, metal bridges are realized on the top of the thin film and connected to the ground sides of the CPW line using via holes (see Fig. 1). The layout of the 4 × 4 array is shown in Fig. 2. The metal plane is truncated $0.53\lambda_o$ away from the array, where $\lambda_o$ is the free-space wavelength at 25 GHz. Since the feeding CPW is barred under the BCB layer, contact pads are patterned on the top of the BCB layer and connected to the edge of the CPW line through via holes. The on-wafer probe used to feed the antenna is placed on the contact pads. A taper is used to accommodate the probe pitch, i.e., 200 $\mu$m, to the pitch of the feeding CPW (see Fig. 2). The cable, probe, and taper are deembedded from the measurements using appropriate calibration standards within the thru-reflection-line (TRL) calibration technique. The design

of the coplanar feeding network is based on the power splitter introduced in [5]. It provides the required 3-dB coupling to both output ports over a wide frequency band without the need of integrating lumped resistors. It depends on coupling the power from the coplanar mode of the feeding CPW in the input port to the "coplanar-like" mode of the triple-slotline section. The triple slotline is split into two CPW lines at the output ports, each of which carrying half of the input power. The $4 \times 4$ array consists of four $2 \times 2$ sub-arrays connected using a coplanar feeding network, as shown in Fig. 2. The four elements of each sub-array are fed using an $H$-resonator [1] instead of a corporate feed. At the resonance frequency of the $H$-resonator, the electrical path difference between the right-hand-side and left-hand-side elements, equals $\lambda_g/2$, where $\lambda_g$ is the wavelength of the coplanar mode of the CPW lines. The resultant $180^\circ$ phase shift between both sides together with $180^\circ$ the spatial rotation, result in co-phased equivalent magnetic currents in both sides. Unlike the $H$-resonator of [1], the resonance frequency of the resonator used here exactly matches that of the dipole antenna. The choice of the $H$-resonator in our case is based on the fact that the $H$-resonator offers a more compact design and more clearance between the network and radiating elements if compared to the corporate feed. It is worth mentioning that the corporate feed offers wider bandwidth than the $H$-resonator. Fig. 3(a) and (b) shows a $2 \times 2$ sub-array of slot dipoles as realized using an $H$-resonator and a corporate feeding network, respectively.

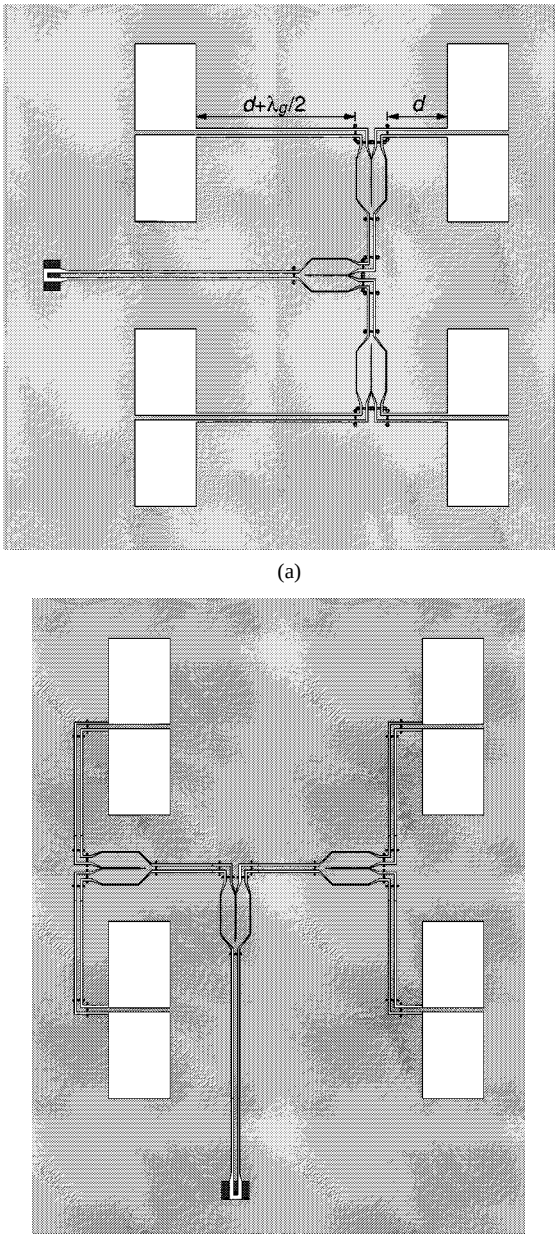


(a)

(b)

Fig. 3. Layout of a $2 \times 2$ sub-array of slot dipoles. (a) Using $H$-resonator. (b) Using corporate feeding network.

## III. Results and Discussions

Figs. 4 and 5 show the measured and calculated return losses versus frequency for the $2 \times 2$ and the $4 \times 4$ array, respectively. The theoretical analysis was carried out using Hewlett-Packard's Momentum, which is a planar solver based on an integral-equation formulation. Very good agreement between theory and measurements is observed for the case of the $2 \times 2$ array. The resonance frequency is predicted within an error of $-0.56\%$. The measured resonance frequency is 24.92 GHz, and the bandwidth for $\mathrm{SWR} < 2$ is 7.2%. It is worth noting that the value of the calculated resonance frequency is strongly dependent on the meshing of the structure [6]. The finer the mesh, the closer the predicted resonance frequency to the measured one. Since Momentum meshes all the elements of the antenna array using subsectional expansion functions, the mesh refinement is possible for the $2 \times 2$ array only. However, for the $4 \times 4$ array, a coarse mesh had to be used, which consumes about 350 Mbytes of the memory, 4036 segments, and requires around 2.5 h for calculating a single frequency point on an HP 9000/782 workstation. Consequently any further mesh refinement for the $4 \times 4$ array is practically impossible. As one would expect, this results in an error in the prediction of the radiating resonance frequency of 2%. However, the main behavior of the $4 \times 4$ array is very well predicted. The measured resonance frequency is 25.08 GHz, and the bandwidth for $\mathrm{SWR} < 2$ is 10%. Comparing these arrays with the microstrip arrays, the conclusion is that they enjoy wide-band behavior without the need of stacking several dielectric layers or using parasitic elements.

The measured and calculated radiation patterns for the $2 \times 2$ and $4 \times 4$ arrays are shown in Figs. 6 and 7, respectively, at the corresponding resonance frequencies. The upper half of each figure represents the radiation pattern in the $H$-plane, the plane normal to the feeding CPW, while the lower half represents the radiation pattern in the $E$-plane. For both planes, the presented results correspond to the backside radiation, which lies below the dielectric substrate in Fig. 1. The front-to-back ratio, as observed from both simulation and experiment, is $-3$ dB. Figs. 6 and 7 show good agreement between theory and measurements. Since the truncation of the metal plane is only $0.53\lambda_o$ away from the antenna arrays, measurements show diffraction patterns interfering with the far-field patterns. This phenomenon is not considered in the simulation, as Momentum always assumes an infinite layer structure. The diffraction is partially due to space-wave diffraction and partially due to surface wave diffraction. Since the $4 \times 4$ array is more directive than the $2 \times 2$ array, the intensity of the space wave at the vicinity of the truncated edge is weaker. Consequently, the space-wave diffraction is less pronounced for the case of the $4 \times 4$ array. This explains that the measured patterns of the $4 \times 4$ array are less sensitive to diffraction than the patterns of the $2 \times 2$ array. From the surface wave point-of-view, the maximum excitation of the surface wave associated with the dipole antenna is in the $E$-plane. As a result, the $E$-plane shows more diffraction than the $H$-plane for both the $2 \times 2$ and the $4 \times 4$ arrays. The important radiation parameters in both principal planes for the $2 \times 2$ and the $4 \times 4$ arrays are summarized in Table I.

In order to calculate the directivity, in the backside broadside direction, the following approximate formula is used [7]:

$$\text{Directivity (dB)} = 10\log_{10}\left(\frac{32\,400}{\Theta_E \Theta_H}\right) - 1.76 \qquad (1)$$

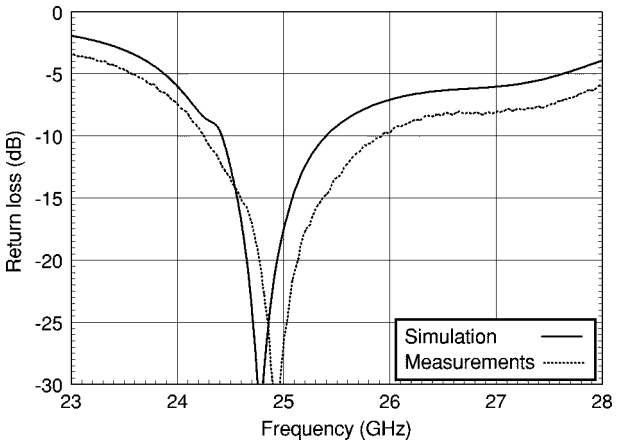


Fig. 4. Return loss versus frequency for the 2 × 2 array.

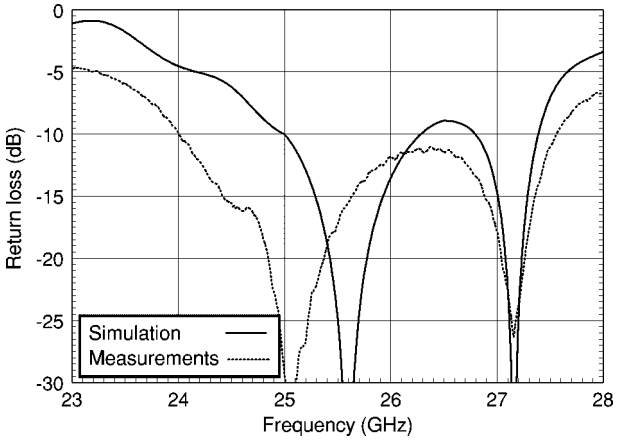


Fig. 5. Return loss versus frequency for the 4 × 4 array.

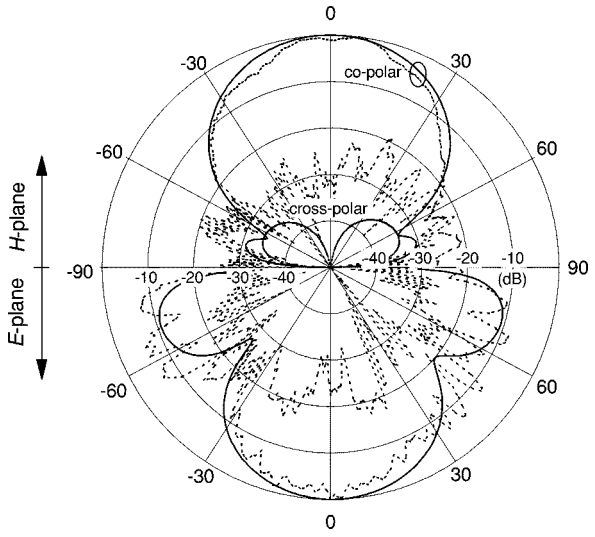


Fig. 6. Radiation patterns of the 2 × 2 array ($f = 24.92$ GHz: upper half represents the $H$-plane, lower half represents the $E$-plane: —— simulation, – - - - - - measurements).

where $\Theta_E$ and $\Theta_H$ are the half-power beamwidths (in degrees) in the $E$- and the $H$-planes, respectively. The subtraction of 1.76 dB is to account for the fact that the backside carries only 2/3 from the total radiated power. Substitute with the half-power beamwidths in (1) results in a broadside backside directivity of 10.24 and 16.3 dB for the 2 × 2 and 4 × 4 arrays, respectively. The measured gain, from the backside, is 10 and 15.7 dB for the 2 × 2 and the 4 × 4 arrays, respectively. Monitoring both the calculated directivity and measured gain indicates that the radiation efficiency is 94.6% and 87% for the 2 × 2 and the 4 × 4 arrays, respectively. These radiation efficiencies are quite good for such planar antennas. The 4 × 4 array shows less radiation efficiency due to the longer feeding network, which suffers from higher conductor losses.

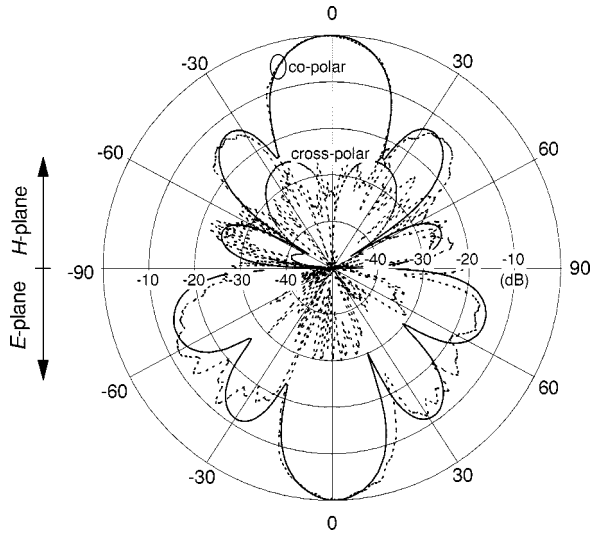


Fig. 7. Radiation patterns of the 4 × 4 array ($f = 25.08$ GHz: upper half represents the $H$-plane, lower half represents the $E$-plane: —— simulation, – - - - - - measurements).

TABLE I
SUMMARY OF THE RADIATION PATTERN PROPERTIES FOR THE 2 × 2 AND THE 4 × 4 ARRAYS

| | | 2×2 array | 4×4 array |
|---|---|---|---|
| Half power beam width | $H$-plane | 46° | 22° |
| | $E$-plane | 44° | 23° |
| Side lobe level (dB) | $H$-plane | −13.4 | −13.4 |
| | $E$-plane | −11.5 | −12 |
| Cross polarization (dB) | $H$-plane | −25 | −26 |
| | $E$-plane | −20 | −30 |

## IV. CONCLUSION

Planar slot antenna arrays in the MCM-D technology have been presented in this paper. The arrays are fed with coplanar feeding networks based on CPW lines. 2 × 2 and 4 × 4 arrays of slot dipoles have been fabricated and fully characterized both theoretically and experimentally. Very good agreement between theory and measurements is observed. The proposed arrays have the advantage of being compatible with the driving electronics, and the integration of active devices and shunt lumped components. Moreover, they enjoy high-impedance bandwidths, low cross-polarization level, high gain, and high radiation efficiency. In order to match the size-reduction requirement in most modern applications, the edges of the metal planes are not very far away from the antenna arrays. This truncation results in a diffraction phenomenon, which is more pronounced for small arrays in the $E$-plane.

## ACKNOWLEDGMENT

The authors would like to thank K. Verhemeldonck, IMEC, Leuven, Belgium, and R. Van Hoof, IMEC, Leuven, Belgium, for their careful

processing of the antenna arrays. The authors also extend many thanks to P. Delmotte, ESAT, Leuven, Belgium, for his assistance during the far-field measurements.

## REFERENCES

[1] H. Legay and L. Shafai, "A self-matching wide-band feed network for microstrip arrays," *IEEE Trans. Antennas Propagat.*, vol. 45, pp. 715–722, Apr. 1997.
[2] P. S. Hall and C. M. Hall, "Coplanar corporate feed effects in microstrip patch array design," *Proc. Inst. Elect. Eng.*, pt. H, vol. 135, pp. 180–186, June 1988.
[3] E. A. Soliman, S. Brebels, G. A. E. Vandenbosch, and E. Beyne, "$X$-band brick wall antenna fed by CPW," *Electron. Lett.*, vol. 34, pp. 836–838, Apr. 1998.
[4] H.-C. Liu, T.-S. Horng, and N. G. Alexopoulos, "Radiation of printed antennas with a coplanar waveguide feed," *IEEE Trans. Antennas Propagat.*, vol. 43, pp. 1143–1148, Oct. 1995.
[5] E. A. Soliman, P. Pieters, E. Beyne, and G. A. E. Vandenbosch, "Suppression of the parasitic modes in CPW discontinuities using MCM-D technology-application to a novel 3-dB power splitter," *IEEE Trans. Microwave Theory Tech.*, vol. 46, pp. 2426–2430, Dec. 1998.
[6] G. A. E. Vandenbosch and A. R. Van de Capelle, "Use of subsectional edge expansion functions (SEEF's) to analyze rectangular microstrip antennas with the method of moments," *Proc. Inst. Elect. Eng.*, pt. H, vol. 139, pp. 159–164, Apr. 1992.
[7] E. Levine, "Special measurement techniques for printed antennas," in *Handbook of Microstrip Antennas*, J. R. James and P. S. Hall, Eds. Stevenage, U.K.: Peregrinus, 1989, ch. 16, p. 991.

# On the Significance of Envelope Peak-to-Average Ratio for Estimating the Spectral Regrowth of an RF/Microwave Power Amplifier

John F. Sevic and Michael B. Steer

***Abstract*—The peak-to-average ratio (PAR) of a signal is commonly used for estimating the backoff required for an radio-frequency/microwave power amplifier to exhibit acceptable intermodulation distortion. In this paper, it is shown that the PAR is an inaccurate metric for predicting the backoff and can lead to improper choices for modulation with respect to the linearity–efficiency tradeoff. A specific case is presented, based on the IS-94 code-division multiple-access communication (CDMA) reverse-link and IS-95 CDMA forward-link wireless standards. Using simulation and load–pull measurements, it is illustrated that although quaternary phase-shift keying has a higher PAR than offset QPSK (O-QPSK), it has lower adjacent-channel power, for constant average power. This observation, contrary to what is expected, is explained by introducing the envelope distribution function, which characterizes the saturation of an amplifier based on the time-domain statistics of the applied signal.**

***Index Terms*—Digital modulation, intermodulation distortion, linearity, microwave power amplifier, peak-to-average ratio, RF power amplifier, signal statistics, spectral regrowth.**

Manuscript received April 14, 1999.

J. F. Sevic is with the Spectrian Corporation, Sunnyvale, CA 94089 USA, and is also with the Institute of Microwaves and Photonics, School of Electrical and Electronic Engineering, The University of Leeds, Leeds LS2 9JT, U.K.

M. B. Steer is with the Institute of Microwaves and Photonics, School of Electrical and Electronic Engineering, The University of Leeds, Leeds LS2 9JT, U.K.

Publisher Item Identifier S 0018-9480(00)04674-3.

## I. INTRODUCTION

Design of digital communication systems often uses the peak-to-average ratio (PAR) of the modulated signal as a qualitative estimate of the tradeoff between the linearity and efficiency of the transmitter stage. At the circuit level, the design of RF/microwave power amplifiers uses the PAR to estimate the load impedance and gatewidth for acceptable intermodulation (IM) distortion and required average output power. For a given average power, the PAR indicates the maximum instantaneous state of saturation of the power amplifier and is, thus, directly related to the IM distortion generated, which, for digitally modulated signals, is manifested as spectral regrowth. Analytical derivation of this relationship is difficult, except for simplistic nonlinearities, and most often one finds that the PAR is used to estimate the required output backoff from the 1-dB single-tone saturation point, particularly for system-level design. Since efficiency decreases as average power is reduced from the saturated-power point, customary application of this metric indicates that a signal with a high PAR would result in lower amplifier efficiency than one with a lower PAR. Thus, from an efficiency perspective, a low PAR modulation would appear to be desirable.

If average IM distortion can be considered as a summation of many instantaneous saturation events, it follows that the resultant average IM distortion must depend on the statistical properties of the signal envelope. The more often an envelope induces saturation, independent of the PAR, then the greater the average IM distortion generated. There are two significant consequences of this observation. The first is that the average IM distortion generated by a power amplifier must depend not only on what the peak power is, as specified by the PAR, but also on the variance of the instantaneous power about the mean power. The second consequence is that since the PAR itself does not characterize how often the associated peak power occurs, it is incapable of characterizing the resultant average IM characteristics. Indeed, it is for these reasons why relating adjacent-channel power ratio (ACPR) to two-tone IM correlation is, in general, difficult since the envelope statistics are vastly different [1].

In this paper, the spectral regrowth properties of QPSK and offset QPSK (O-QPSK) modulated signals used in the IS-94 CDMA reverse-link and IS-95 CDMA forward-link standards, respectively, are compared [2], [3]. It is shown that conventional PAR analysis, which was the basis for choosing O-QPSK for IS-94, underestimates the associated relative spectral regrowth. To describe the statistical nature of the modulated signal, the envelope distribution function is introduced. This function describes the probability of a peak-power occurring and, hence, the frequency of instantaneous compression of the power amplifier. The envelope distribution function illustrates why spectral regrowth of QPSK, using IS-95 filtering, has lower spectral regrowth than similarly filtered O-QPSK, contrary to what is expected using the PAR. Spectral regrowth simulations of a submicrometer laterally diffused MOS (LDMOS) transistor, under power loading with strong class-AB bias, are used to confirm the predictions of the envelope distribution function. In addition, load–pull measurements of a similar LDMOS transistor, under linearity–efficiency loading and weak class-AB bias, are given, verifying the simulated results under different operating conditions.

## II. GENERATION OF DIGITALLY MODULATED SIGNALS AND THE ENVELOPE DISTRIBUTION FUNCTION

Simulation of spectral regrowth is now commonplace; the two most common methods being harmonic-balance envelope-related methods

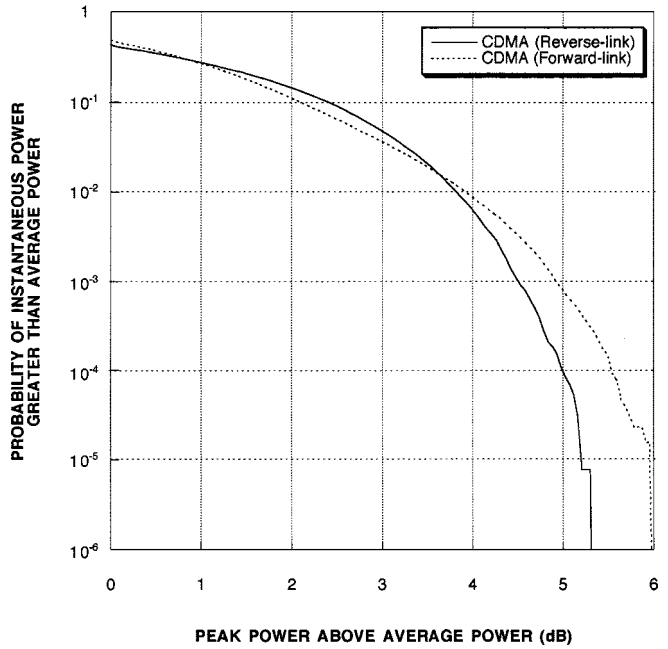


Fig. 1. Envelope distribution functions for IS-95 QPSK and IS-94 O-QPSK modulation.

and behavioral-model-related methods[1] [4]–[6]. Since data sequence correlation and filtering each impact the envelope statistics, it is necessary that the signal used in the simulation be identical to that used in the load–pull characterization [7]. The digitally modulated signals used for the present experiment were generated using a proprietary method with the HP Circuit Envelope simulator. The complex envelope from this source was downloaded to an arbitrary waveform generator coupled to a vector signal generator, thus providing the digitally modulated signal for load–pull characterization.

To simplify filtering, the sampling rate of the source was set equal to four times the chip rate specified by the IS-94/IS-95 standards, which is the sampling rate of the associated filter. The length of the pilot-tone spreading sequence was approximated using $2^9$ b, with the maximal length sequence (MLS) coefficients and seed values specified by IS-94 [2], [3]. Although this sequence is not as long as the period of the spreading-sequence given in IS-94, it has been found to be statistically identical with respect to stationarity [8].

Representative envelope distribution functions for IS-95 QPSK and IS-94 O-QPSK modulated signals, derived from simulation, are shown in Fig. 1. The envelope distribution function is defined as the probability that the instantaneous power is greater than the average power

$$\Psi(\tilde{p}) = 1 - \int_{E[\tilde{p}]}^{\infty} \varphi(\tilde{p})\, d\tilde{p} \tag{1}$$

where $E[\tilde{p}]$ is the average power of the complex envelope $\tilde{p}(t)$ and $\varphi(\tilde{p})$ is the probability density function of $\tilde{p}(t)$. The PAR is defined as the $x$-axis intercept at a probability of $10^{-6}$. Using this definition, the PAR's for IS-95 QPSK and IS-94 O-QPSK are 6.1 and 5.1 dB, respectively, and these are the commonly used values. Since the probability of these peak powers occurring is extremely low, it is obvious that the PAR is not a reliable metric for estimating the efficiency and linearity tradeoff of an RF/microwave power amplifier since the occurrence of an instantaneous saturation event is very unlikely. Instead, Fig. 1 indicates that the IM distortion of a power amplifier under QPSK modulation should be better than that with O-QPSK since the envelope distribution function for QPSK rolls off faster in regions of high probability of peak power, i.e., it has a smaller variance in regions of high probability.

[1]Microwave Design System, version b.07.10, Hewlett-Packard Company, Palo Alto, CA 1997.

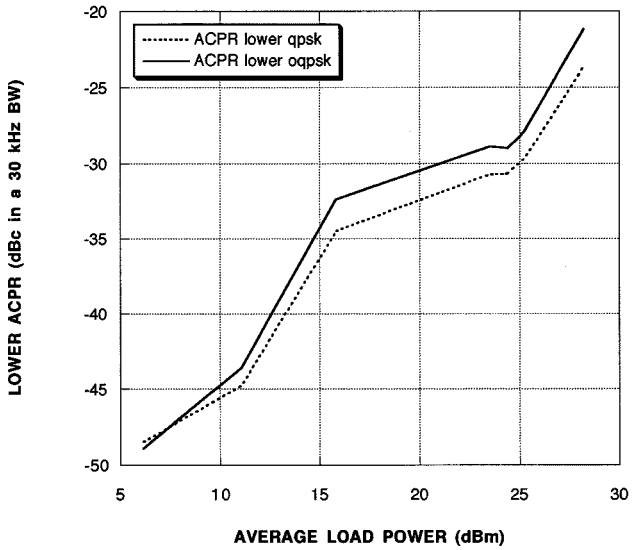


Fig. 2. Simulated lower ACPR for IS-95 QPSK and IS-94 O-QPSK modulation (computed at an offset of 885 kHz normalized to the total channel power).

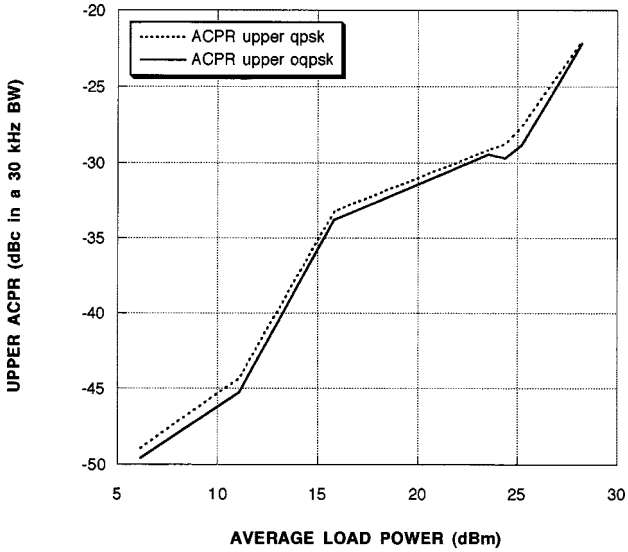


Fig. 3. Simulated upper ACPR for IS-95 QPSK and IS-94 O-QPSK modulation (computed at an offset of 885 kHz normalized to the total channel power).

## III. Nonlinear Simulation and Load–Pull Characterization of Spectral Regrowth

A large-signal table-based model was extracted from a unit-cell submicrometer LDMOS transistor and was scaled to match the device used in the load–pull characterization. Large-signal verification of the model confirmed acceptable accuracy. The transistor used in the simulation was biased at 4.0 V and 8 mA/mm under maximum power loading, with a carrier frequency of 850 MHz. Figs. 2 and 3 compare simulated lower and upper ACPR's, respectively, for QPSK and O-QPSK excitation. These ACPR's were computed by taking the ratio of the power in a 30-kHz bandwidth, at an offset of 885 kHz, to the total channel power,

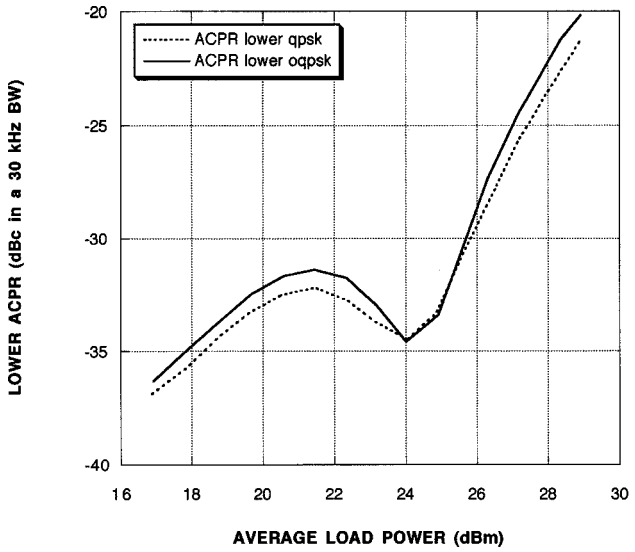


Fig. 4. Measured lower ACPR for IS-95 QPSK and IS-94 O-QPSK modulation (computed at an offset of 885 kHz normalized to the total channel power).

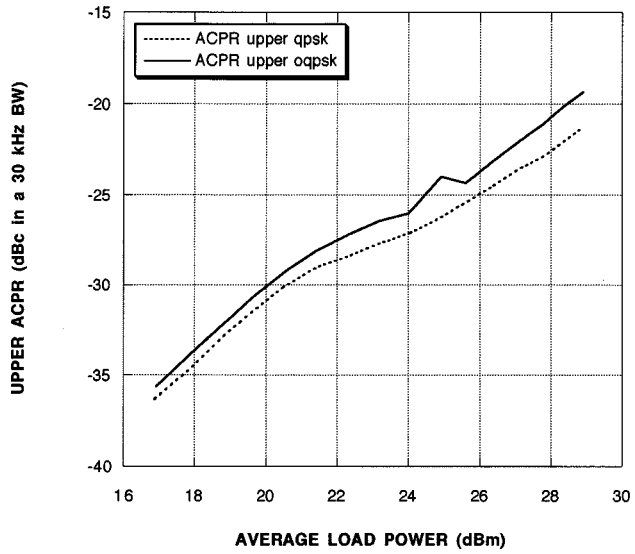


Fig. 5. Measured upper ACPR for IS-95 QPSK and IS-94 O-QPSK modulation (computed at an offset of 885 kHz normalized to the total channel power).

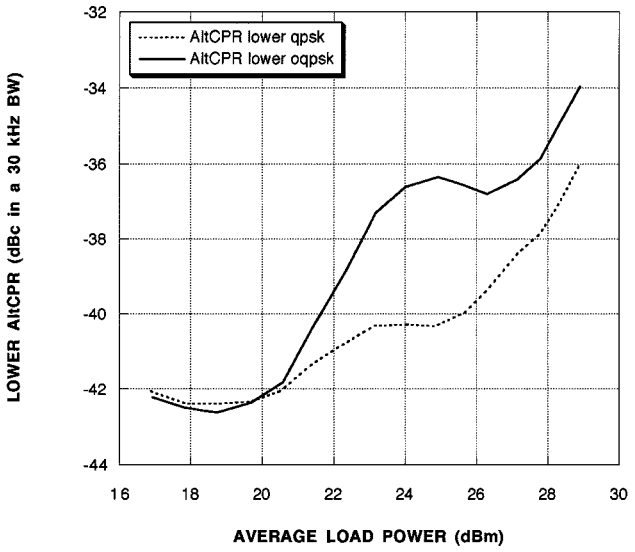


Fig. 6. Measured lower AltCPR for IS-95 QPSK and IS-94 O-QPSK modulation (computed at an offset of 1250 kHz normalized to the total channel power).

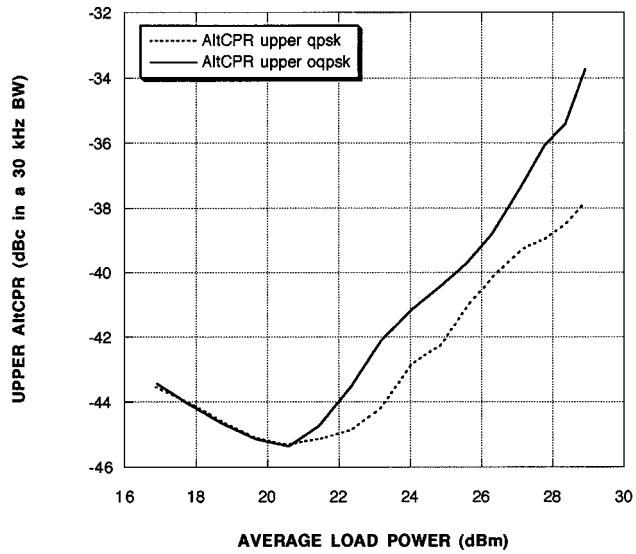


Fig. 7. Measured upper AltCPR for IS-95 QPSK and IS-94 O-QPSK modulation (computed at an offset of 1250 kHz normalized to the total channel power).

using the procedure described in [7]. While the simulated upper QPSK and O-QPSK ACPR's are similar, the lower QPSK ACPR is better than the O-QPSK ACPR by 2 dB from the linear region of the power amplifier well into compression. This behavior is directly attributable to the properties of the envelope distribution function for QPSK, as described in the previous section.

The absence of IM nulling in the simulation is due to inadequate modeling of the envelope termination and the strong class-AB bias of 8 mA/mm [9]. In the simple simulation presented here, the envelope impedance was set to the fundamental frequency impedance. In addition, the quiescent current was chosen higher than what would normally be used to examine the effect of bias current on the linearity relationship between QPSK and O-QPSK. The measured results, presented next, use a more conventional quiescent current of 4 mA/mm.

A transistor identical to the one used in the simulation was evaluated in a Maury load–pull system, with source and load impedances chosen for optimal linearity–efficiency loading. This was done to further examine the sensitivity of the spectral regrowth relationship between QPSK and O-QPSK under different bias and source/load conditions. The transistor was biased at 4.0 V and 4 mA/mm with a frequency of 850 MHz. An arbitrary waveform generator, using data generated from the simulation, was used to drive a vector signal source, which was directly applied to the load–pull system.

Figs. 4 and 5 compare lower and upper ACPR's, respectively, for QPSK and O-QPSK excitation. Two distinctions can be made between the simulated and measured results. First, unilateral IM nulling is evident in the lower ACPR. Since nulling is not evident in the upper ACPR, the ACPR exhibits asymmetry, which is attributable to the envelope termination effect [9]. The difference in QPSK and O-QPSK ACPR is slightly less than the simulation predicted, although QPSK again exhibits better linearity than O-QPSK.

Figs. 6 and 7 compare lower and upper alternate-channel power ratio (AltCPR), respectively, for QPSK and O-QPSK excitation, measured at

TABLE I
COMPARISON OF MEASURED ACPR AND AltCPR FOR QPSK AND O-QPSK AT AN AVERAGE LOAD POWER OF 28 dBm (NOTE THAT THIS DEVICE WOULD NOT BE ACCEPTABLE FOR USE IN A TYPICAL CDMA HANDSET PA)

| RATIO | QPSK | O-QPSK | IMPROVEMENT |
|---|---|---|---|
| Upper ACPR | -23.0 dB | -21.0 dB | 2.0 dB |
| Lower ACPR | -23.5 dB | -22.6 dB | 1.1 dB |
| Upper AltCPR | -39.1 dB | -36.0 dB | 3.1 dB |
| Lower AltCPR | -37.2 dB | -35.5 dB | 2.2 dB |

an offset of 1250 kHz [7]. AltCPR also exhibits asymmetry, though the asymmetry is much weaker for QPSK than O-QPSK. QPSK AltCPR is 2–3 dB better than O-QPSK.

Table I summarizes the results for an average load power of 28 dBm. The measured results exhibit an identical trend in spectral regrowth performance to that observed in the simulations. Thus, even under different source/load and bias conditions, QPSK exhibits lower spectral regrowth than O-QPSK. This result is in contradiction to that predicted by PAR's of QPSK and O-QPSK. That is, based on PAR considerations alone, ACPR and AltCPR of QPSK signals would be expected to be much higher than for O-QPSK signals. In fact, just the opposite is observed.

## IV. CONCLUSION

A quantitative study of spectral regrowth for QPSK and O-QPSK, representative of the IS-94 and IS-95 CDMA wireless standards, has been presented in this paper. Both nonlinear simulation and measured results indicate that O-QPSK offers no advantage over QPSK in the linearity–efficiency tradeoff of an RF/microwave power amplifier, as would have been predicted using conventional PAR analysis. This perspective, while counter-intuitive in the context of PAR, follows naturally from the envelope distribution function.

The envelope distribution function was introduced as a new figure-of-merit, and clearly illustrates why QPSK, although exhibiting a higher PAR than O-QPSK, exhibits lower spectral regrowth. Although not shown in this paper, simulations using IS-54 $\pi/4$-QPSK showed that even with a low PAR of 3.4 dB, the spectral regrowth was larger than similarly filtered QPSK, with a PAR of 4.2 dB. Thus, the conclusions presented are of a general nature, and are not specific to one type of modulation. This new function should find wide application in the design of modulations for optimizing the linearity–efficiency tradeoff of RF/microwave power amplifiers used in digital wireless communication systems.

## ACKNOWLEDGMENT

The authors wish to thank the reviewers for their many helpful suggestions.

## REFERENCES

[1] J. F. Sevic, M. B. Steer, and A. M. Pavio, "Large-signal automated load–pull of adjacent-channel power for digital wireless communication systems," in *IEEE MTT-S Int. Microwave Symp. Dig.*, June 1996, pp. 763–766.

[2] *Mobile Station-Base Station Compatibility Standard for Dual-Mode Wide-Band Spread Spectrum Cellular System*, EIA/TIA Interim Standard TIA/EIA/IS-94, 1993.

[3] *Mobile Station-Base Station Compatibility Standard for Dual-Mode Wide-Band Spread Spectrum Cellular System*, EIA/TIA Interim Standard TIA/EIA/IS-95, 1993.

[4] J. F. Sevic and J. Staudinger, "Simulation of adjacent-channel power ratio for digital wireless systems," in *IEEE Veh. Technol. Conf. Dig.*, May 1997, pp. 681–685.

[5] K. Gard, H. M. Gutierrez, and M. B. Steer, "Characterization of spectral regrowth in microwave amplifiers based on the nonlinear transformation of complex Gaussian process," *IEEE Trans. Microwave Theory Tech.*, vol. 47, pp. 1059–1069, July 1999.

[6] E. Ngoya and R. Larcheveque, "Envelope transient analysis: A new method for the transient and steady-state analysis of microwave communication circuits and systems," in *IEEE MTT-S Int. Microwave Symp. Dig.*, June 1996, pp. 1365–1368.

[7] J. F. Sevic, M. B. Steer, and A. M. Pavio, "Nonlinear analysis methods for digital wireless communication systems," *Int. J. Microwave Millimeter-Wave Computer-Aided Eng.*, pp. 197–216, May 1996.

[8] J. F. Sevic, "Characterization and simulation of RF/microwave power transistors using digitally modulated signals," in *1998 Fall ARFTG Short-Course Notes*, Dec. 1998.

[9] J. F. Sevic, K. Burger, and M. B. Steer, "A novel load–pull technique for mitigation of envelope-induced ACPR asymmeetry of RF power amplifiers," in *IEEE MTT-S Int. Microwave Symp. Dig.*, June 1998, pp. 601–605.

# Three-Dimensional Microwave Tomography: Experimental Imaging of Phantoms and Biological Objects

Serguei Y. Semenov, Alexander E. Bulyshev, Alexandre E. Souvorov, Alexei G. Nazarov, Yuri E. Sizov, Robert H. Svenson, Vitaly G. Posukh, Andrey Pavlovsky, Pavel N. Repin, and George P. Tatsis

***Abstract*—Microwave tomographic experiments have been performed on a three-dimensional (3-D) phantom and excised canine heart using a 3-D system operating at frequency of 2.4 GHz. A modified gradient reconstruction approach has been employed for the 3-D image reconstruction. To compare two-dimensional (2-D) and 3-D approaches, we also performed 2-D image reconstruction using an approach based on the Newton method. Experimental data acquired on experimental phantoms were analyzed using both 2-D and 3-D reconstruction approaches. High-quality images were reconstructed using the 3-D approach. The reconstruction procedure failed when the 2-D approach was applied to reconstruct images of the 3-D object. An image of the dielectrical properties of the excised canine heart was obtained using a 3-D reconstruction approach. Images successfully revealed a complex internal structure of the heart, including both right-hand side and left-hand side ventricles.**

***Index Terms*—Biophysical experiment, imaging, microwave tomography.**

Manuscript received June 2, 1999. This work was supported by the Carolinas HealthCare System Foundation through the Carolinas Medical Center, Carolinas Heart Institute under a grant.

S. Y. Semenov, A. E. Bulyshev, A. E. Souvorov, R. H. Svenson, and G. P. Tatsis are with the Laser and Applied Technologies Laboratory, Carolinas Heart Institute, Carolinas Medical Center, Charlotte, NC 28203 USA.

A. G. Nazarov, A. Pavlovsky, and P. N. Repin are with the Biophysical Laboratory, Kurchatov Institute of Atomic Energy, Moscow, Russia.

Y. E. Sizov is with the Troitsk Institute of Innovative and Thermonuclear Research, Troitsk, Moscow Region, Russia.

V. G. Posukh is with the Institute of Laser Physics, Novosibirsk, Russia.

Publisher Item Identifier S 0018-9480(00)04675-5.

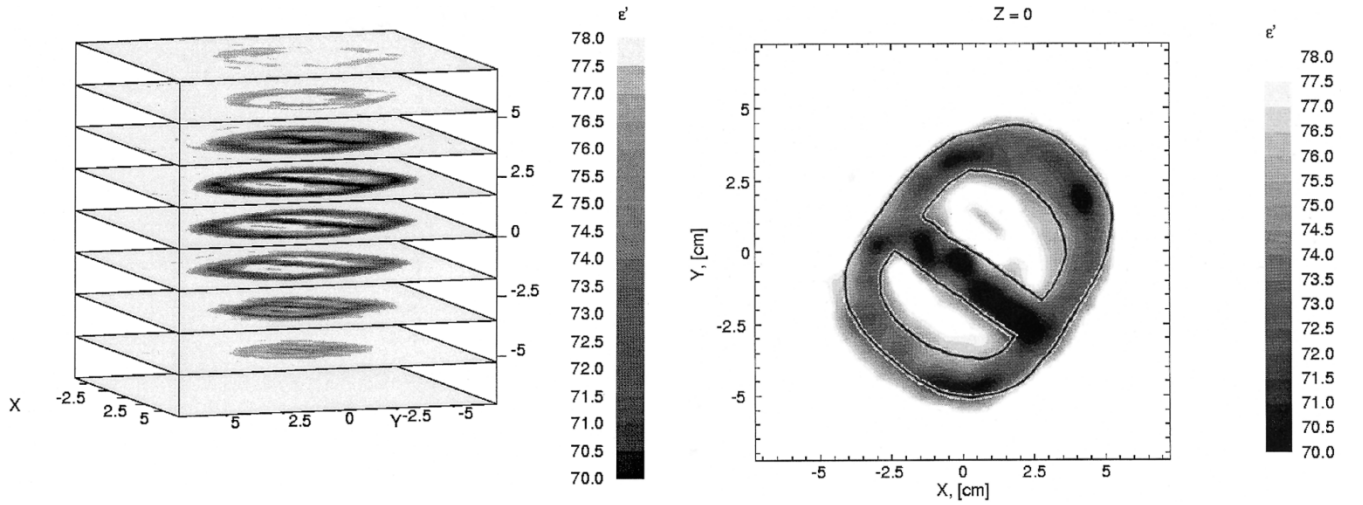


(a) (b)

Fig. 1. (a) Reconstructed image of a 3-D phantom using a 3-D approach. (b) Cross section $Z = 0$.

## I. Introduction

The microwave tomographic problem has been extensively studied during the last decade [1]–[6]. The reason for this is because this method potentially has enormous advantages for diagnostic imaging in medicine [7], [8], including an imaging of physiological and pathological conditions of tissues. For example, we have demonstrated that dielectrical properties of myocardial tissue depend on blood content, acute ischemia, and chronic infarction [9]. Other research groups [10] have shown that dielectrical properties of breast cancer tissue are significantly different from normal breast tissue.

Significant milestones have been achieved in two-dimensional (2-D) geometry, including an imaging of high contrast and full-scale objects [11] and attempts to image biological objects [3], [8, pp. 127–174]. In the last cases, some information about internal structure and dielectrical properties of three-dimensional (3-D) biological objects was achieved. This raised a question as to what extent a 2-D approach of microwave tomography can be applied to obtain an image of a 3-D objects. The first objective of this paper is to compare results of reconstruction of 3-D objects using 2-D and 3-D approaches.

Using a developed 3-D microwave tomographic system and 3-D reconstruction method for imaging of low-contrast objects, we achieved images of 3-D phantoms with low-contrast of dielectrical properties [12]. To obtain images of 3-D objects with high-contrast of dielectrical properties, we generalized the gradient method into the 3-D case [13]. The second objective of this paper is to obtain a 3-D image of the excised static canine heart.

## II. Experimental Setup

Experiments were conducted using the 3-D microwave tomographic system operating at a frequency of 2.4 GHz. The system description and procedure of conducting the tomographic experiments are described elsewhere [12]. In this study, an object to be imaged was hooked up to a rotating plate on the axis of the cylindrical tomographic working chamber. The dimensions of the chamber were 40 cm in height and 60 cm in diameter. The transmitter was located at a 17.3-cm distance from the center of the tomographic chamber. Its position did not changed during the experiment. To obtain a full set of tomographic data, we rotated the object under study and positioned the receiving antenna at various points ($14 \times 32$) on a semicylinder with a radius of 11.5 cm and a height of $\pm 10$ cm behind the object. The accurate position of the receiving antenna was conducted with the help of an automatic motion system and motion control system. The object under study was rotated $11.2^{\circ}$ in azimuthal angle and, consequentially, totally irradiated from 32 directions. The dimension of an array of acquired data was $14 \times 32 \times 32$.

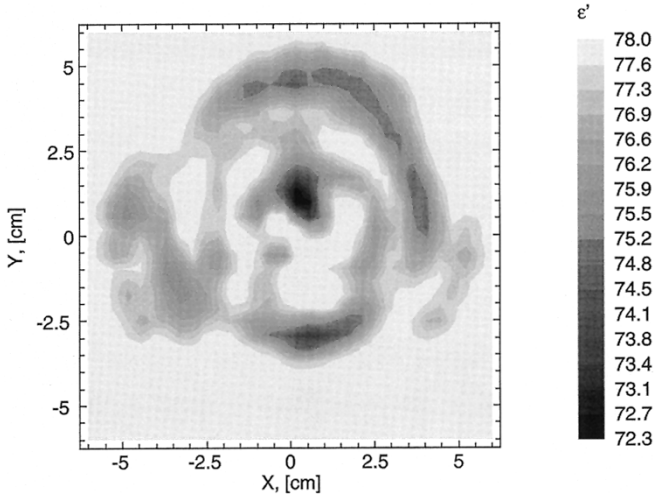


Fig. 2. Reconstructed images of 3-D phantom using 2-D approach. Cross section $Z = 0$.

The microwave tomographic chamber was filled with deionized water with $\varepsilon = 78 + j10$. To measure dielectrical properties of materials and solutions, we used a standard coaxial probe method and a HP8753-D Network Analyzer. In addition, on-line temperature control of the solution in the working chamber was used during experiments.

Physiological procedure was previously described in [3].

## III. Image Reconstruction Method

To obtain 2-D images, we used a reconstruction approach [11] based on the Newton method. This approach allows us to obtain both high-quality experimental and simulated images in 2-D geometry [11], including high-contrast and large-scale objects. In this study, the direct problem was solved on a fine mesh of 128 nodes over an azimuthal angle of 64 nodes over radius. The inverse problem was solved in a Cartesian mesh of 46 nodes $\times$ 46 nodes.

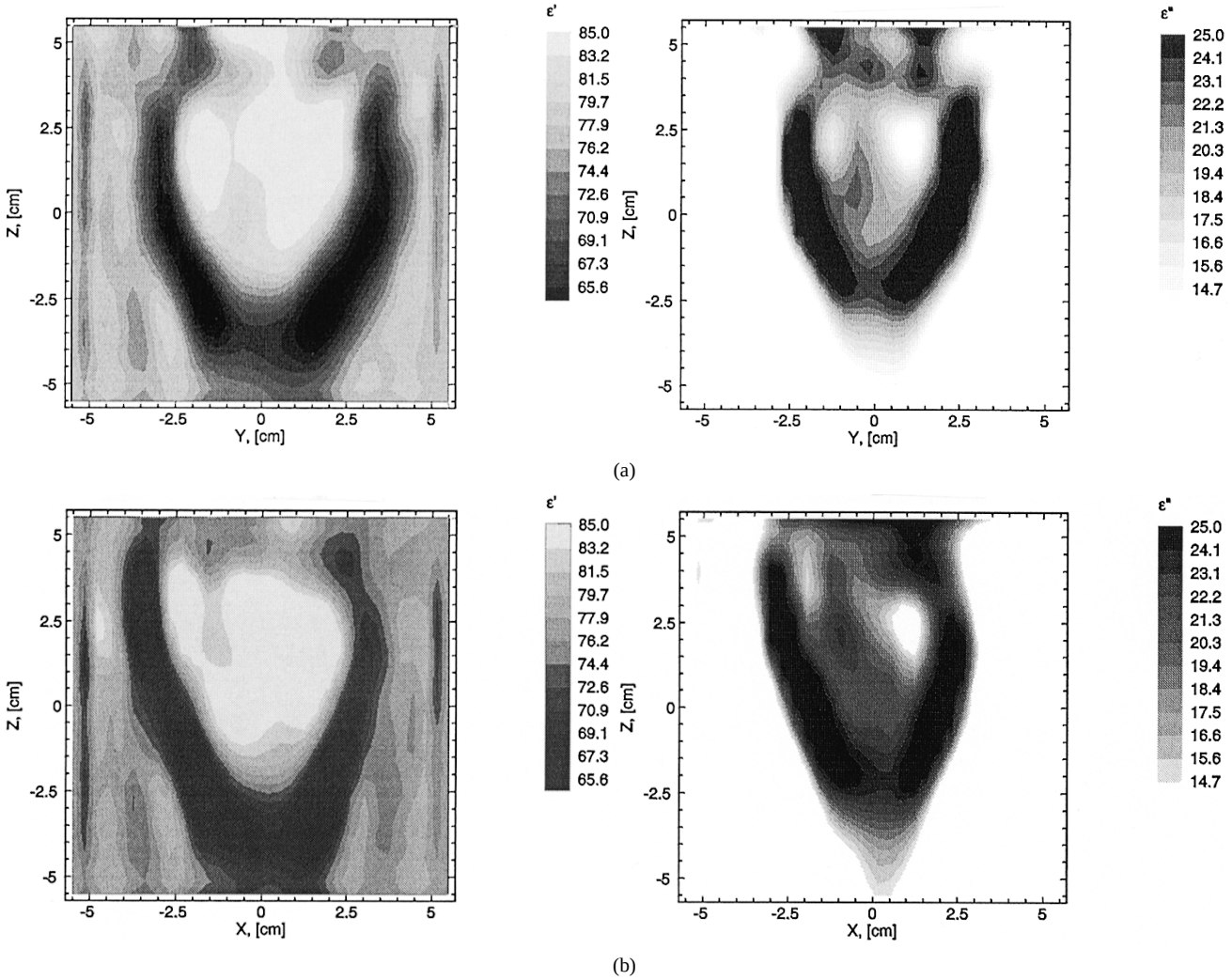


Fig. 3. Reconstructed images of excised canine heart. (a) Cross section $X = 1.5$ cm. (b) Cross section $Y = 1.5$ cm.

To obtain 3-D images, we used an approach based on the gradient method [14] generalized into the 3-D case [13]. The direct problem was solved on a fine mesh of 256 nodes over an azimuthal angle of 128 nodes over radius and 128 nodes over the vertical direction in the cylindrical coordinate system. The inverse problem was solved in a Cartesian mesh of 64 nodes $\times$ 64 nodes $\times$ 64 nodes. All calculations were performed on a DEC ALPHA-8200 server.

## IV. Results and Discussion

The first part of this experimental study was conducted using a 3-D phantom. The phantom was an ellipsoid with two asymmetric holes, which simulated the heart ventricular chambers. The tomographic chamber and phantom chambers were filled with deionized water with $\varepsilon = 78 + j10$. The dielectrical properties of phantom materials (foam soaked with water) were $\varepsilon = 70 + j9$. In this experiment, the imaginary part of the phantom dielectrical permittivity was chosen to be close to that of water, therefore, an imaging of the real part of the dielectrical permittivity was expected. Fig. 1 (3-D sliced on the top and 2-D cross section in central area) reveals a shape that is very close to the shape of the phantom (black contour). The real part of the dielectrical properties was properly reconstructed.

Furthermore, to compare results of reconstruction of 3-D objects using 2-D and 3-D approaches, the same experimental data, acquired in a central 2-D cross section, were used for obtaining an image using a 2-D reconstruction approach. The results of reconstruction are presented in Fig. 2. As can be seen, the reconstruction of the internal structure fails. Only an external boundary of the phantom can be seen. This clearly shows the importance of using a 3-D approach of diffraction tomography, including microwave tomography, to reconstruct images of 3-D objects.

In this paper, we used a 3-D reconstruction approach to obtain images of an excised static canine heart. The reconstructed image of an excised static canine heart is presented in Fig. 3. The dielectrical properties of myocardium were about $\varepsilon = 60 + j17$ at room temperature. The tomographic chamber and heart chambers were filled with deionized water with $\varepsilon = 78 + j10$. Two different vertical cross sections are shown. Both real and imaginary parts of complex dielectrical permittivity were reconstructed. Presented images reflect structural complexity of the heart. Left- and right-hand-side ventricles are clearly seen. The values of reconstructed dielectrical permittivity are similar to, but do not quite agree with, dielectrical properties of myocardium.

Earlier [3], we used a 2-D approach for image reconstruction of both static and beating canine hearts. Some information about imaged object was obtained. However, recent images clearly demonstrate the im-

portance of the 3-D approach for imaging 3-D biological objects; the images presented reveal much better quality as compared with previously reconstructed images of a canine heart using a 2-D reconstruction procedure based on iterations of a Rytov approximation. For example, both heart ventricles are clearly seen and separated.

## V. Conclusion

Microwave tomographic experiments have been performed on a 3-D phantom and excised canine heart using a 3-D system operating at frequency of 2.4 GHz. Experimental data acquired on the experimental phantom were analyzed using both 2-D and 3-D reconstruction approaches. High-quality images were reconstructed using the 3-D approach. The reconstruction procedure failed when the 2-D approach was used for reconstruction of a 3-D object. Images of dielectrical properties of an excised static canine heart were obtained using a 3-D reconstruction approach. Images successfully revealed a complex internal structure of the heart, including both right- and left-hand-side ventricles.

## References


[1] J. C. Bolomey and C. Pichot, "Some applications of diffraction tomography to electromagnetics—The particular case of microwaves," in *Inverse Problems in Scattering and Imaging*, M. Bertero and E. R. Pike, Eds. New York: Adam Hilger, 1992, pp. 319–344.

[2] W. C. Chew and Y. M. Wang, "Reconstruction of two-dimensional permittivity distribution using the distorted Born iterative method," *IEEE Trans. Med. Imag.*, vol. 9, pp. 218–225, Feb. 1990.

[3] S. Y. Semenov, R. H. Svenson, A. E. Bulyshev, A. E. Souvorov, V. Y. Borisov, Y. E. Sizov, A. N. Starostin, K. R. Dezern, G. P. Tatsis, and V. Y. Baranov, "Microwave tomography: Two-dimensional system for biological imaging," *IEEE Trans. Biomed. Eng.*, vol. 43, no. 9, pp. 869–877, 1996.

[4] P. M. Meaney, K. D. Paulsen, A. Hartov, and R. K. Crane, "Microwave imaging for tissue assessment: Initial evaluation of multitarget tissue-equivalent phantoms," *IEEE Trans. Biomed. Eng.*, vol. 43, pp. 878–890, Sept. 1996.

[5] N. Joachimowicz, C. Pichot, and J. Hugonin, "Inverse scattering: An iterative numerical method for electromagnetic imaging," *IEEE Trans. Antennas Propagat.*, vol. 39, pp. 1742–1752, Dec. 1991.

[6] M. S. Hawley, A. Broquetas, L. Jofre, J. C. Bolomey, and G. Gaboriaud, "Microwave imaging of tissue blood content changes," *J. Biomed. Eng.*, vol. 13, pp. 197–202, May 1991.

[7] L. E. Larsen and J. H. Jacobi, Eds., *Medical Applications of Microwave Imaging*. New York: IEEE Press, 1986.

[8] M. Myakawa and J. C. Bolomey, Eds., *Non-Invasive Thermometry of the Human Body*. Boca Raton, FL: CRC Press, 1996.

[9] S. Y. Semenov, R. H. Svenson, and G. P. Tatsis, "Microwave spectroscopy of myocardial ischemia and infarction. 1. Experimental study," *Ann. Biomed. Eng.*, to be published.

[10] W. T. Joines, Y. Zhang, C. Li, and R. L. Jirtle, "The measured electrical properties of normal and malignant human tissues from 50 to 900 MHz," *Med. Phys.*, vol. 21, no. 4, pp. 547–550, Apr. 1994.

[11] A. E. Souvorov, A. E. Bulyshev, S. Y. Semenov, R. H. Svenson, A. G. Nazarov, Y. E. Sizov, and G. P. Tatsis, "Microwave tomography: A two-dimensional Newton iterative scheme," *IEEE Trans. Microwave Theory Tech.*, vol. 46, pp. 1654–1659, Nov. 1998.

[12] S. Y. Semenov, R. H. Svenson, A. E. Bulyshev, A. E. Souvorov, A. G. Nazarov, Y. E. Sizov, A. Pavlovsky, V. Y. Borisov, B. G. Voinov, G. Simonova, A. N. Starostin, G. P. Tatsis, and V. Y. Baranov, "Three-dimensional microwave tomography: Experimental prototype of the system and vector Born reconstruction method," *IEEE Trans. Biomed. Eng.*, vol. 46, pp. 937–946, Aug. 1999.

[13] A. E. Bulyshev, S. Y. Semenov, A. E. Souvorov, R. H. Svenson, A. G. Nazarov, Y. E. Sizov, and G. P. Tatsis, "Three dimensional microwave tomography. Computer experiments," *Inverse Problems*, to be published.

[14] R. Kleinman and P. van der Berg, "A modified gradient method for two-dimensional problems in tomography," *J. Comput. Appl. Math.*, vol. 42, p. 17, 1992.


# Improved Design for Symmetrical Six-Port Microstrip Coupler (Based on Double-Ring-with-Star Topology)

S. P. Yeo, B. Tan, and E. H. Kwek

***Abstract*—Other researchers have designed a symmetrical six-port microstrip coupler that yields a bandwidth of 7%. It has been found in this paper that a change of the design topology allows the coupler's bandwidth to be increased. A simple-to-use computer model of the double-ring-with-star prototype has also been developed and tests have confirmed that good agreement can be expected between the predicted and measured results.**

***Index Terms*—Microstrip components.**

## I. Introduction

As Judah *et al.* [1] have pointed out, various implementations have already been reported for six-port couplers with the following scattering matrix:

$$\underline{S}_{\text{ideal}} = \begin{bmatrix} 0 & \alpha_o & 0 & \tau_o & 0 & \alpha_o \\ \alpha_o & 0 & \alpha_o & 0 & \tau_o & 0 \\ 0 & \alpha_o & 0 & \alpha_o & 0 & \tau_o \\ \tau_o & 0 & \alpha_o & 0 & \alpha_o & 0 \\ 0 & \tau_o & 0 & \alpha_o & 0 & \alpha_o \\ \alpha_o & 0 & \tau_o & 0 & \alpha_o & 0 \end{bmatrix} \tag{1}$$

where $|\alpha_o| = |\tau_o| = 1/\sqrt{3}$ and $\arg(\alpha_o/\tau_o) = \pm 2\pi/3$. Examples of such couplers can be found in [2]–[4]; recognizing, however, that "... none of these are either broadband or planar and are thus not widely used" [1, p. 109]. Judah *et al.* have instead chosen the symmetrical six-port microstrip coupler (based on the single-ring-with-star topology) as the core component of a novel six-port reflectometer that is capable of yielding optimum measurement performance.

In an earlier paper [5], we utilized the basic transmission-line approach to model a similar six-port coupler based on the simpler single-ring topology. Subsequent studies have since indicated that it is not possible for us to design a prototype with a sufficiently wide bandwidth if we limit ourselves to the single-ring topology (either on its own, as in [5], or with the central star, as in [1]); e.g., the coupler developed by Judah *et al.* has a VSWR bandwidth of only 7% [1]. Therefore, this has prompted us to explore the feasibility of other design topologies.

As depicted in Fig. 1, the prototype we finally obtained (after having tested a number of different structures) combines the double-ring topology attempted by Kim *et al.* [6] for another related coupler (i.e., symmetrical five-port coupler) and the central star adopted by Judah *et al.* [1] for their narrow-band design of the six-port coupler. In addition, we have introduced angular displacements of $\pi/6$ for the six ring-to-ring links (instead of aligning them with the spokes of the central star and the external arms leading to the connectors).

## II. First-Order Analysis

We note from the preliminary results reported in [1] and [5] that the scattering matrix of the symmetrical six-port microstrip coupler should, in general, be written in the following manner (based on the sixfold

Manuscript received July 23, 1999.

The authors are with the Electrical Engineering Department, National University of Singapore, Kent Ridge, Singapore 119260.

Publisher Item Identifier S 0018-9480(00)04676-7.

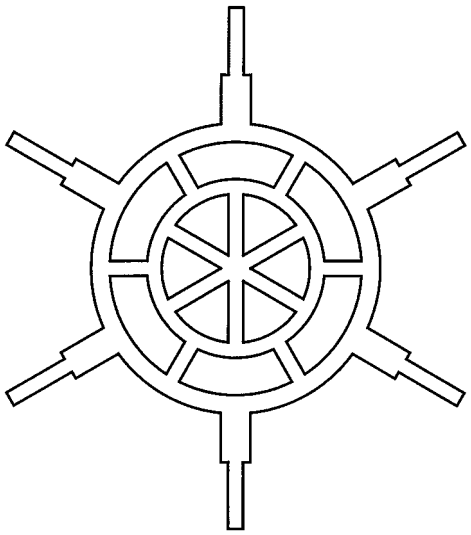

Fig. 1. Prototype for symmetrical six-port microstrip coupler based on double-ring-with-star topology. Inner ring: width of 0.8 mm and radius of 10.9 mm. Outer ring: width of 2.1 mm and radius of 15.4 mm. Central star: width of 4.6 mm and length of 10.5 mm. Ring-to-ring links: width of 0.8 mm and length of 3.4 mm. Step transformers: width of 2.1 mm and length of 11.6 mm. External lines: width of 1.5 mm. Substrate: relative permittivity of 10.1 and height of 1.6 mm.

rotational symmetry of the overall structure):

$$\underline{S}_{\text{actual}} = \begin{bmatrix} \gamma & \alpha & \beta & \tau & \beta & \alpha \\ \alpha & \gamma & \alpha & \beta & \tau & \beta \\ \beta & \alpha & \gamma & \alpha & \beta & \tau \\ \tau & \beta & \alpha & \gamma & \alpha & \beta \\ \beta & \tau & \beta & \alpha & \gamma & \alpha \\ \alpha & \beta & \tau & \beta & \alpha & \gamma \end{bmatrix}. \tag{2}$$

For a reasonably well-designed prototype, which yields scattering-coefficient values that are not far from what have been specified in (1), the entries of $\underline{S}_{\text{actual}}$ can be expressed as first-order departures from the corresponding entries of $\underline{S}_{\text{ideal}}$ as follows:

$$\gamma = \Delta_\gamma \exp j\phi_\gamma \tag{3}$$

$$\beta = \Delta_\beta \exp j\phi_\beta \tag{4}$$

$$\alpha = \left(\frac{1}{\sqrt{3}} + \Delta_\alpha\right) \exp j(\phi_\alpha + \delta_\alpha) \tag{5}$$

$$\tau = \left(\frac{1}{\sqrt{3}} + \Delta_\tau\right) \exp j(\phi_\tau + \delta_\tau). \tag{6}$$

If we assume that losses are not significant, the expressions of (3)–(6) may then be substituted into the unitary-matrix equation $\underline{S}^*{}_{\text{actual}}\underline{S}_{\text{actual}} = \underline{I}$, which, when simplified, will provide us with the following interrelationships among the unknown first-order terms $\Delta_\gamma$, $\Delta_\beta$, $\Delta_\alpha$, $\Delta_\tau$, $\delta_\alpha$, and $\delta_\tau$:

$$\Delta_\tau = -2\Delta_\alpha \tag{7}$$

$$|\delta_\tau - \delta_\alpha| = 3\Delta_\alpha \tag{8}$$

$$\Delta_\gamma \cos(\phi_\gamma - \phi_\tau) = -2\Delta_\beta \cos(\phi_\beta - \phi_\alpha) \tag{9}$$

$$\Delta_\gamma \cos(\phi_\gamma - \phi_\alpha) = -\Delta_\beta \Big\{ \cos(\phi_\beta - \phi_\alpha) + \cos(\phi_\beta - \phi_\tau) \Big\}. \tag{10}$$

It is evident from (7) and (8) that the departures of $\alpha$ and $\tau$ from their ideal-case values are related to each other: if there is an increase of $\Delta_\alpha$ in $|\alpha|$, then $|\tau|$ will decrease by $2\Delta_\alpha$ and $\arg(\tau/\alpha)$ will increase by $3\Delta_\alpha$. Equally interesting is the observation that both of these equations do not contain any of the other terms in $\gamma$and $\beta$, thus suggesting that the behavior of $\alpha$ and $\tau$ for any reasonably well-designed symmetrical six-port coupler is not affected by any first-order departures of $\gamma$ and $\beta$ from their common ideal-case setting of zero; for the converse situation, however, we may not presume that $\Delta_\alpha$, $\Delta_\tau$, $\delta_\alpha$, and $\delta_\tau$ will be negligibly small when we are given a prototype with zero mismatch (i.e., $\gamma = 0$) and excellent isolation (i.e., $\beta = 0$).

Equations (9) and (10), on the other hand, portray a different picture for the near-zero coefficients of $\gamma$ and $\beta$: the settings for the coupling-coefficient phases $\phi_\alpha$ and $\phi_\tau$ have to be taken into account when determining the values of $\gamma$ and $\beta$. To solve (9) and (10) (for, say, $\Delta_\beta$ and $\phi_\beta$ in terms of $\Delta_\gamma$ and $\phi_\gamma$), we need to introduce an additional equation that specifies the location of the terminal planes at the six ports of the coupler. If we select $\phi_\alpha + \phi_\tau = 0$ as the ancillary equation (as in [7]), the solution of these homogeneous equations will then yield the following relationships:

$$\Delta_\beta = \Delta_\gamma \sqrt{\sin^2\phi_\gamma + \frac{\cos^2(\phi_\gamma - \phi_\alpha)}{4\cos^2\phi_\alpha}} \tag{11}$$

$$\tan\phi_\beta = \frac{-2\sin\phi_\gamma \cos\phi_\alpha}{\cos(\phi_\gamma - \phi_\alpha)}. \tag{12}$$

## III. Prototype Coupler

Instead of resorting to an empirical cut-and-try procedure (which is rather laborious in view of the number of parameters that are available for us to adjust), we have decided to develop an easy-to-use model that can be incorporated into a computer-aided-design software package. As mentioned earlier in Section I, the details for the analysis of the simpler coupler with single-ring topology have already been reported in [5]. Our present coupler employs the more complicated structure depicted in Fig. 1 and, thus, we need to expand on the basic analysis initiated in [5] so as to account for the various additional features (i.e., second concentric ring, links between the two rings, star at the center, and step discontinuities at the external arms). The resultant equations we have derived for the eigen-admittance $\hat{Y}_m$ of the composite coupler when operating in eigenmode of order $m$ (where $m = 0, 1, 2, 3$) are listed in detail in (13)–(18), shown at the bottom of this page (where the subscripts "ring1" and "ring2" refer to the outer and inner rings, respectively).

The microstrip formulas furnished in Hoffman's handbook [8] can be used for computing the numerical values of the various line and junction parameters appearing in (13)–(18) at the bottom of the following page: $Y$ (characteristic admittance of line), $\theta$ (electrical angle of either curved arc joining adjacent ports or straight link between rings), $n$ (transformer ratio associated with tee junction), $B$ and $L$ (shunt susceptances at tee junction and step discontinuity, respectively). Also required are the formulas enumerated in [5] for evaluating the scattering coefficients of (2) after we have utilized (13)–(18) to compute the four unique eigen-admittances $\hat{Y}_m$ (where $m = 0, 1, 2, 3$) of the coupler.

The optimization software we thereafter developed employs the genetic algorithm outlined in [9] to minimize the following error function (summed over all sample frequency points $f_k$):

$$\Delta = \sum_{k=1}^{k=K} \left\{ w_\gamma |\gamma(f_k)|^2 + w_\beta |\beta(f_k)|^2 + w_\alpha \left[ |\alpha(f_k)| - \frac{1}{\sqrt{3}} \right]^2 + w_\tau \left[ |\tau(f_k)| - \frac{1}{\sqrt{3}} \right]^2 \right\}. \tag{19}$$

We have found from the experience gained in running our computer-aided-design software that improved results may be achieved when we

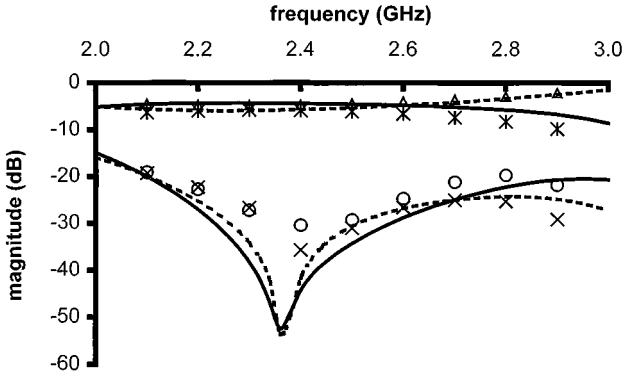


Fig. 2. Magnitudes of scattering coefficients for prototype coupler (with structure and dimensions given in Fig. 1). $|\gamma|$: o o o (measured), —— (predicted). $|\beta|$: x x x (measured), - - - - - (predicted). $|\alpha|$: * * * (measured), —— predicted). $|\tau|$: $\Delta\ \Delta\ \Delta$ (measured), - - - - - (predicted).

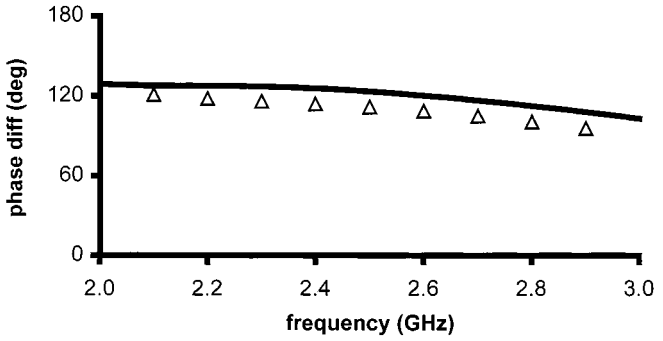


Fig. 3. Phase difference between coupling coefficients $\tau$ and $\alpha$ for prototype coupler (with structure and dimensions given in Fig. 1). $\Delta\ \Delta\ \Delta$ (measured), —— (predicted).

choose $w_\gamma = w_\alpha = 1.5 w_\beta = 0.5 w_\tau = 1$ (in view of the observations noted earlier in Section II) instead of simply resorting to the standard setting of equal values for all four weights.

The results presented in Fig. 2 confirm that the prototype coupler we produced is able to satisfy the design specifications reasonably well (i.e., $|\gamma| < 0.1, |\beta| < 0.1$ and $\||\alpha| - |\tau|\| < 0.1$) over the 2.1–2.75-GHz range; in comparison, we note that for the prototype of Judah *et al.* "the fractional bandwidth over which $|s_{11}| < -20$ dB is approximately 7%" [1, p. 115], but the coupling bandwidth is comparable with that achieved in Fig. 2. Furthermore, the good agreement between predicted and experimental data indicates that the simplifications we incorporated into our model (e.g., approximating curved arcs between adjacent ports as straight lengths of transmission line and disregarding effect of parasitic coupling between discontinuities) have not seriously impaired the accuracy of our numerical results over the frequency range of interest to us—not only for scattering-coefficient magnitudes (Fig. 2), but also for phase differences (Fig. 3).

## IV. Conclusions

As suggested by Kim *et al.*, we have found it useful to "... add a generalized compensating circuit which has couplings between the adjacent ports" [6, p. 54] so as to increase the bandwidth of the symmetrical six-port microstrip coupler to more than 25% (with $|\gamma| < 0.1, |\beta| < 0.1$ and $\||\alpha| - |\tau|\| < 0.1$). We have also developed two simplified models to help us during the design process—a first-order model [which assists us in our choice of suitable settings for the weights $w_\gamma$, $w_\alpha$, $w_\beta$, and $w_\tau$ of (19)]and an eigenmode model (which, as is evident from the results of Figs. 2 and 3, is able to predict the values of the coupler's scattering coefficients).

As a final note, we wish to add that our resultant computer-aided-design software (which is compact enough to be run on a Pentium PC)

$$\hat{Y}_m = \frac{(\hat{Y}_m)_A}{1 + j\omega L_{\text{step}} (\hat{Y}_m)_A} \tag{13}$$

where

$$(\hat{Y}_m)_A = Y_{\text{step}} \frac{(\hat{Y}_m)_B + jY_{\text{step}} \tan\theta_{\text{step}}}{Y_{\text{step}} + j(\hat{Y}_m)_B \tan\theta_{\text{step}}} \tag{14}$$

$$(\hat{Y}_m)_B = \frac{jY_{\text{ring1}}}{n_{\text{ring1}}} \left\{ \frac{2Y_{\text{ring1}} \left[\cos\left(\frac{m\pi}{3}\right) - \cos\theta_{\text{ring1}}\right] - j(\hat{Y}_m)_C \sin\theta_{\text{ring1}}}{Y_{\text{ring1}} \sin\theta_{\text{ring1}} + j(\hat{Y}_m)_C \sin^2\left(\frac{1}{2}\ \theta_{\text{ring1}}\right)} + B_{\text{ring1}} \right\} \tag{15}$$

$$(\hat{Y}_m)_C = n_{\text{link}} Y_{\text{link}} \frac{(\hat{Y}_m)_D + jY_{\text{link}} \tan\theta_{\text{link}}}{Y_{\text{link}} + j(\hat{Y}_m)_D \tan\theta_{\text{link}}} + jB_{\text{link}} \tag{16}$$

$$(\hat{Y}_m)_D = \frac{jY_{\text{ring2}}}{n_{\text{ring2}}} \left\{ \frac{2Y_{\text{ring2}} \left[\cos\left(\frac{m\pi}{3}\right) - \cos\theta_{\text{ring2}}\right] - j(\hat{Y}_m)_E \sin\theta_{\text{ring2}}}{Y_{\text{ring2}} \sin\theta_{\text{ring2}} + j(\hat{Y}_m)_E \sin^2\left(\frac{1}{2}\ \theta_{\text{ring2}}\right)} + B_{\text{ring2}} \right\} \tag{17}$$

$$(\hat{Y}_m)_E = \begin{cases} jn_{\text{star}} Y_{\text{star}} \tan\theta_{\text{star}} + jB_{\text{star}}, & \text{for } m = 0 \\ jn_{\text{star}} Y_{\text{star}} \cot\theta_{\text{star}} + jB_{\text{star}}, & \text{for } m = 1, 2, 3. \end{cases} \tag{18}$$

is able to yield couplers with other specifications as well (e.g., $|\gamma| = 0$ and $|\alpha| = |\beta| = |\tau| = 1/\sqrt{5}$ for five-way power division, as reported in [10]). This can be readily achieved by amending those few program lines in the software that define the error function $\Delta$ of (19).

## REFERENCES


[1] S. K. Judah, M. J. Page, and M. Judd, "Planar symmetrical six-port junction," *Proc. Inst. Elect. Eng.*, pt. H, vol. 134, pp. 109–115, Apr. 1987.

[2] A. L. Cullen, S. K. Judah, and F. Nikravesh, "Impedance measurement using a six-port directional coupler," *Proc. Inst. Elect. Eng.*, pt. H, vol. 127, pp. 92–98, Apr. 1980.

[3] A. L. Cullen, "The six-port in microwave measurements," in *European Microwave Conf. Dig.*, 1979, pp. 74–82.

[4] C. R. Boyd, "On a class of multiple-line directional couplers," *IRE Trans. Microwave Theory Tech.*, vol. MTT-10, pp. 287–293, July 1962.

[5] S. P. Yeo and C. L. Lau, "First-order model of symmetrical six-port microstrip ring coupler," *IEEE Trans. Microwave Theory Tech.*, vol. 39, pp. 1666–1669, Sept. 1991.

[6] D. I. Kim, K. Araki, and Y. Naito, "Properties of symmetrical five-port circuit and its broad-band design," *IEEE Trans. Microwave Theory Tech.*, vol. MTT-32, pp. 51–57, Jan. 1984.

[7] A. J. Belfort and A. L. Cullen, "First-order theory of five-port symmetrical star junction," *Electron. Lett.*, vol. 18, pp. 841–842, Sept. 1982.

[8] R. K. Hoffmann, *Handbook of Microwave Integrated Circuits*. Norwood, MA: Artech House, 1987.

[9] M. Gen and R. Cheng, *Genetic Algorithm and Engineering Design*. New York: Wiley, 1996.

[10] G. P. Riblet and E. R. B. Hansson, "Some properties of the matched symmetrical six-port junction," *IEEE Trans. Microwave Theory Tech.*, vol. MTT-32, pp. 164–171, Feb. 1984.


# Chiral Hard-Surface Waveguide Mode Transformer

Ari J. Viitanen

***Abstract*—Field propagation in cylindrical axially corrugated waveguide filled with chiral medium is considered in this paper. The depth of the corrugation is a quarter-wavelength, making a hard-surface (HS) boundary. The eigenfields inside the chiral HS waveguide are circularly polarized. In a nonchiral HS waveguide, these eigenmodes are propagating with the same propagation factor. However, for small chirality values, there exists weak coupling between the eigenfields, which results in a change in polarization of the propagating field. This effect makes it possible to make mode transformers and phase shifters. Also, the chiral HS waveguide of a proper length can be used as a matching element between different kinds of circular waveguides.**

***Index Terms*—Chiral media, hard-surface waveguide, mode transformer.**

## I. INTRODUCTION

Propagation of fields inside a cylindrical chiral waveguide with a corrugated boundary is considered in this paper. The corrugated waveguides are used in antenna techniques since, in such structures, circularly polarized waves are propagating [1]. The corrugation in this paper is in the axial direction and the depth of the corrugation is a quarter-wavelength. The boundary condition of this kind of waveguide is equivalent to the boundary condition on a hard surface (HS), defined in [2]. It is known that, in this kind of waveguide, TEM fields are propagating [2]. In this paper, the HS waveguide is filled with chiral medium, and higher order modes are considered. The wave propagation in different kinds of chirowaveguides have been considered in [3]–[5]. Waveguides with impedance walls are especially considered in [6], of which the HS waveguide is a special case. Inside waveguides filled with chiral medium, there are two propagating partial waves, i.e., right- and left-side circularly polarized fields, denoted by $+$ and $-$ fields. With high values of the chirality parameter, these two eigenfields are decoupled in the HS waveguide, but for small values of the chirality parameter, the fields are slightly coupled, which causes a change in polarization for the propagating field. A couple of applications are given, which are based on the coupling effect between the eigenfields.

Manuscript received December 9, 1999.

The author is with the Electromagnetics Laboratory, Helsinki University of Technology, FIN-02015 HUT, Finland.

Publisher Item Identifier S 0018-9480(00)04664-0.

## II. EIGENFIELDS

The time–harmonic fields of the form $e^{j\omega t}$ are considered. The special direction of the boundary, i.e., the direction of the corrugation, is parallel to the $z$-axis, and the fields depend on $z$ as $e^{-j\beta z}$, where the propagation factor $\beta$ is a real number. The waveguide is filled with isotropic chiral medium with the constitutive relations [7]

$$\boldsymbol{D} = \epsilon \boldsymbol{E} - j\kappa\sqrt{\mu_o\epsilon_o}\boldsymbol{H} \quad \boldsymbol{B} = \mu \boldsymbol{H} + j\kappa\sqrt{\mu_o\epsilon_o}\boldsymbol{E} \tag{1}$$

where $\epsilon$ is the permittivity, $\mu$ is the permeability, and $\kappa$ is the chirality parameter of the medium. For a lossless chiral medium, all the material parameters $\epsilon$, $\mu$, and $\kappa$ are real numbers. Electric and magnetic fields are written with the transverse and axial parts as $\boldsymbol{E} = \boldsymbol{e} + E_z\boldsymbol{u}_z$ and $\boldsymbol{H} = \boldsymbol{h} + H_z\boldsymbol{u}_z$ and are inserted into the Maxwell equations

$$\nabla \times \boldsymbol{E} = -j\omega\boldsymbol{B} \quad \nabla \times \boldsymbol{H} = j\omega\boldsymbol{D}. \tag{2}$$

The fields in chiral medium can be expressed in terms of right- and left-hand circularly polarized waves denoted by $+$ and $-$ waves, respectively [6], [7]. After eliminating the transverse fields $\boldsymbol{e}$ and $\boldsymbol{h}$, and using the decomposition into $+$ and $-$ parts, the Maxwell equations finally reduce to the Helmholtz equation for the axial partial fields

$$\left[\nabla_t^2 + k_{c\pm}^2\right] E_{z\pm}(\rho, \varphi) = 0 \tag{3}$$

where

$$E_{z\pm} = \frac{1}{2}\left(E_z \mp j\eta H_z\right)$$

$$k_{c\pm} = \sqrt{k_\pm^2 - \beta^2}$$

and

$$k_\pm = k \pm k_o\kappa.$$

The $\nabla_t$ operator is the transverse part of $\nabla$. The solutions of the Helmholtz equation in cylindrical coordinates are Bessel functions of the first kind

$$E_{z\pm}(\rho, \varphi) = A_{n\pm}J_n(k_{c\pm}\rho)e^{jn\varphi}. \tag{4}$$

All the other field components can be expressed with these two axial field components. The coefficients $k_{c\pm}$ and $A_{n\pm}$ are determined by the boundary and initial conditions, respectively.

The partial transverse fields are obtained from the axial parts as

$$\boldsymbol{e}_\pm = \left[-\frac{j\beta}{k_{c\pm}^2}\nabla_t \mp \frac{k_\pm}{k_{c\pm}^2}\boldsymbol{u}_z \times \nabla_t\right] E_{z\pm}. \tag{5}$$

These two partial transverse fields $\boldsymbol{e}_+$ and $\boldsymbol{e}_-$ are elliptically polarized of opposite handedness with respect to the direction of propagation in

the waveguide. The total fields are obtained as combinations of transverse and axial partial fields as

$$\boldsymbol{E} = \boldsymbol{e}_+ + \boldsymbol{e}_- + (E_{z+} + E_{z-})\boldsymbol{u}_z \tag{6}$$

and

$$\boldsymbol{H} = \frac{j}{\eta}\left[\boldsymbol{e}_+ - \boldsymbol{e}_- + (E_{z+} - E_{z-})\boldsymbol{u}_z\right]. \tag{7}$$

Parameters $k_{c\pm}$ are determined by the boundary condition for the HS at $\rho = a$ [2]

$$\boldsymbol{u}_z \cdot \boldsymbol{E} = 0 \quad \boldsymbol{u}_z \cdot \boldsymbol{H} = 0 \tag{8}$$

which leads to the eigenvalue equation

$$J_n(k_{c+}a)J_n(k_{c-}a) = 0. \tag{9}$$

The solution of the eigenvalue equation is

$$k_{c\pm} = \frac{p_{ns}}{a} \tag{10}$$

where $p_{ns}$ are the values when the Bessel functions vanish. This results in different solutions since the propagation factors $\beta_\pm = \sqrt{k_\pm^2 - (p_{ns}/a)^2}$ are different for $+$ and $-$ waves. This means that, inside the HS waveguide, the eigenmodes with the same index $n$ are always decoupled when the waveguide is filled with chiral material. For a nonchiral case, the two circularly polarized fields are degenerate, i.e., the eigenwaves are propagating with the same propagation factor $\beta$. However, for small chirality parameter values, the coupling of the eigenwaves is weak.

## III. Mode Transformation Effect

The polarization properties of fields propagating inside a chiral HS waveguide are considered when the chirality of the medium is weak. Chiral media with a small chirality parameter value are practically interesting. Chiral media can be fabricated by inserting small helices into the base material [7]. The chirality parameter $\kappa$ is proportional to the density of chiral inclusions. However, high density of inclusions increases losses and may cause problems in practical applications. In this paper, the required chirality parameter is small and can be achieved with a small density of inclusions. Indeed, in case of weakly chiral media, the chirality parameter can be approximated as a real value directly proportional to the frequency. Permittivity and permeability can be approximated as constants in a wide frequency range, as the inclusions are far from the resonance [8].

Denoting the wavenumbers of the partial waves in chiral medium as $k_\pm = k(1 \pm \kappa_r)$ with $\kappa_r = \kappa\sqrt{\mu_o\epsilon_o/\mu\epsilon}$ and assuming that $|\kappa_r| \ll 1$, the propagation factors are approximated as

$$\beta_\pm = \sqrt{k^2(1 \pm \kappa_r)^2 - \left(\frac{p_{ns}}{a}\right)^2} \approx \beta \pm \frac{k^2}{\beta}\kappa_r \tag{11}$$

where the parameters $\beta = \sqrt{k^2 - k_c^2}$ and $k_c = p_{ns}/a$ are the same as for the nonchiral waveguide. The axial field components now reduce to the form

$$E_{z\pm} \approx A_{n\pm}J_n(k_c\rho)e^{jn\varphi}e^{-j\beta z}e^{\mp j(k^2/\beta)\kappa_r z}. \tag{12}$$

Similarly, the transverse partial waves are written as a function of the axial components and approximated as

$$\boldsymbol{e}_\pm \approx \left[-\frac{j\beta}{k_c^2}\nabla_t \mp \frac{k}{k_c^2}\boldsymbol{u}_z \times \nabla_t\right] E_{z\pm}(\rho, \varphi, z). \tag{13}$$

Denoting at $z = 0$ the axial field components as $E_z(0) = A_{n+} + A_{n-} = E_n$ and $H_z(0) = (j/\eta)(A_{n+} - A_{n-}) = H_n$, , the axial electric-field component is

$$E_z(z) = \left[E_n \cos\left(\frac{k^2}{\beta}\kappa_r z\right) - \eta H_n \sin\left(\frac{k^2}{\beta}\kappa_r z\right)\right] \cdot J_n(k_c\rho)e^{jn\varphi}e^{-j\beta z} \tag{14}$$

and the axial magnetic-field component is

$$H_z(z) = \left[H_n \cos\left(\frac{k^2}{\beta}\kappa_r z\right) + \frac{E_n}{\eta}\sin\left(\frac{k^2}{\beta}\kappa_r z\right)\right] \cdot J_n(k_c\rho)e^{jn\varphi}e^{-j\beta z}. \tag{15}$$

The mode transformation effect is clearly seen in these expressions. If, for example, at $z = 0$ the axial field component $H_n = 0$, there exists only an axial electric field, but no axial magnetic field, we have $\mathrm{TM}_{ns}$ fields. The index $ns$ is the corresponding mode index. At the distance when $z$ is

$$z = \frac{\pi\beta}{2k^2\kappa_r} \tag{16}$$

which is denoted by $\lambda_p/4$, there exists the axial magnetic-field component, but no axial electric-field component, which means that there exist only $\mathrm{TE}_{ns}$ fields, thus, the TM mode is transformed to the TE mode. Similarly, the TE mode can be transformed to the TM mode with a section of $\lambda_p/4$ chiral HS waveguide.

When the length of the chiral HS waveguide is twice the value of (16), the field configuration is at 180° phase shift of its original value. Thus, the chiral HS waveguide of length $\lambda_p/2$ between two normal HS waveguide works as a 180° phase shifter.

In the general case, inside the HS waveguide, there are propagating hybrid modes, a combination of TE and TM fields. Actually, by choosing the length of the chiral HS waveguide properly, the original hybrid mode field propagating in an HS waveguide can be transformed to any other hybrid mode.

## IV. Impedance Transformer

As the axial field components are known, the total transverse fields can be obtained by using (13) as $\boldsymbol{e} = \boldsymbol{e}_+ + \boldsymbol{e}_-$ and $\boldsymbol{h} = (j/\eta)(\boldsymbol{e}_+ - \boldsymbol{e}_-)$. Considering the transverse fields in the case when at $z = 0$, the coefficient $H_n = 0$, it is also found that the corresponding wave impedance $\overline{\overline{Z}}$ defined as

$$\boldsymbol{e} = -\overline{\overline{Z}} \cdot \boldsymbol{h} \tag{17}$$

is changed from TM impedance $\overline{\overline{Z}}(0) = \eta(\beta/k)\overline{\overline{J}}$ to TE impedance $\overline{\overline{Z}}(\lambda_p/4) = \eta(k/\beta)\overline{\overline{J}}$ at $z = \lambda_p/4$. At other points, the impedance dyadic is

$$\overline{\overline{Z}}(z) = \eta\,\frac{\dfrac{\beta^2 - k^2}{2}\sin\left(2\,\dfrac{k^2}{\beta}\kappa_r z\right)\overline{\overline{I}}_t + \beta k\overline{\overline{J}}}{k^2\cos^2\left(\dfrac{k^2}{\beta}\kappa_r z\right) + \beta^2\sin^2\left(\dfrac{k^2}{\beta}\kappa_r z\right)} \tag{18}$$

where $\overline{\overline{I}}_t$ is a transverse unit dyadic and $\overline{\overline{J}} = \boldsymbol{u}_z \times \overline{\overline{I}}$ is a 90° rotator. Similarly, when at $z = 0$, $E_n = 0$, one obtains the expression for the TE impedance $\overline{\overline{Z}}(0) = \eta(k/\beta)\overline{\overline{J}}$, which is transformed to the following impedance dyadic at point $z$:

$$\overline{\overline{Z}}(z) = \eta\,\frac{-\dfrac{\beta^2 - k^2}{2}\sin\left(2\,\dfrac{k^2}{\beta}\kappa_r z\right)\overline{\overline{I}}_t + \beta k\overline{\overline{J}}}{k^2\sin^2\left(\dfrac{k^2}{\beta}\kappa_r z\right) + \beta^2\cos^2\left(\dfrac{k^2}{\beta}\kappa_r z\right)}. \tag{19}$$

After the distance $\lambda_p/4$, this is the expression for the TM impedance. In a general case, with the nonzero values of $H_n$ and $E_n$ at $z = 0$, the impedance dyadic for a hybrid mode is obtained, which can be transformed to an impedance dyadic of another hybrid mode with a proper length of the chiral HS waveguide. This is an impedance transformer, which can be used as a matching component between different kinds of waveguides.

## V. Properties of Propagating Fields

Inside an HS waveguide, different kinds of waves can propagate, e.g., TEM fields, circularly polarized fields, TE and TM fields, and combinations of these fields [1], [2]. The propagating modes depend on the excitation of the fields inside the HS waveguide. As the HS waveguide is connected to the chiral HS waveguide, the right- and left-hand polarized fields suffer a phase shift, which depends on the length of the chiral HS waveguide. The phase shift is of the opposite sign for right- and left-hand polarized fields. For TE and TM modes, this effect causes mode transformation between TE and TM polarizations.

Let us generally consider the fields propagating inside the HS waveguide. The expressions for axial components of the fields at $z = 0$ are

$$E_z(0) = E_n J_n(k_c\rho)e^{jn\varphi}$$
$$H_z(0) = H_n J_n(k_c\rho)e^{jn\varphi} \tag{20}$$

which vanish on the boundary of HS waveguide according to the boundary condition. When taking $H_n = 0$, the mode is $\mathrm{TM}_{ns}$. The field configuration of this mode is exactly the same as inside the circular waveguide with a perfect electric conductor (PEC) wall. Similarly, when taking the $\mathrm{TE}_{ns}$ mode, i.e., $E_n = 0$, the field configuration is the same as for the circular waveguide with a perfect magnetic conductor (PMC) wall [9].

TM fields propagating inside the circular PEC waveguide are transformed inside the chiral HS waveguide of length $\lambda_p/4$ to TE fields, as was presented in the previous section. The field configuration of the transformed fields are similar to the fields inside the circular PMC waveguide. These fields can propagate in HS waveguide, but not in PEC waveguide. When the length of the chiral HS waveguide is $\lambda_p/2$, the transformed fields are TM fields, but have suffered a 180° phase shift. In this case, the transformed fields are able to propagate in PEC waveguide. To avoid reflections at interfaces between different kinds of waveguides, the values of the wave impedances should also be matched.

Applications of the chiral HS waveguide between two nonchiral HS waveguides are a mode transformer between TE and TM modes and phase shifters considered in the previous section. In addition, the chiral HS waveguide of length $\lambda_p/2$ may be used as a 180° phase shifter between two circular PEC waveguides for TM modes. One can also use chiral HS waveguide to produce propagating fields similar to those propagating in a circular PMC waveguide. Therefore, the chiral HS waveguide of length $\lambda_p/4$ can be used as a matching element between the PEC waveguide and an open dielectric waveguide with high permittivity or to connecting the PEC waveguide to a dielectric rod antenna.

Another type of application is based on the field properties at high frequency. $\beta \to k$ and the impedance dyadic then reduces to the impedance of a plane wave $\overline{\overline{Z}} = \eta\overline{\overline{J}}$. The total fields are almost transverse, e.g., the electric field is

$$\boldsymbol{e}(\rho, \varphi, z) = \left[\cos(k_o\kappa z)\overline{\overline{I}}_t - \sin(k_o\kappa z)\overline{\overline{J}}\right] \cdot \boldsymbol{e}(\rho, \varphi, 0)e^{-jkz}. \tag{21}$$

The field pattern is rotating during propagation by an angle $k_o\kappa z$ counterclockwise when $\kappa > 0$ and clockwise when $\kappa < 0$ with respect to propagation direction. This effect is similar to the plane-wave propagation in unbounded chiral medium [7]. The chiral HS waveguide can be used at high frequency as a reciprocal twist element for rotating the field pattern by a certain angle.

## VI. Conclusion

Fields propagating in slightly chiral HS waveguide were considered in this paper. It is found that with small chirality parameter values, the polarization of the propagating wave is changed. If the length of the chiral HS waveguide is $\lambda_p/4$, the propagating TM mode is transformed to TE mode and vice versa. If the length of the chiral HS waveguide is $\lambda_p/2$, the field pattern suffers a 180° phase shift. In the general case, the propagating hybrid mode can be transformed to another hybrid mode by a chiral HS waveguide of a proper length. If a circular waveguide with metal conductor boundary is connected to a $\lambda_p/4$ chiral HS waveguide, the TM mode is transformed to the TE mode, but the fields now satisfy the boundary condition on the magnetic conductor. This may be used as a matching element between the metal-wall circular waveguide and an open dielectric waveguide with high permittivity or a dielectric rod antenna.

## References


[1] P. J. B. Clarricoats and A. D. Olver, *Corrugated Horns for Microwave Antennas*. Stevenage, U.K.: Peregrinus, 1984.

[2] P.-S. Kildal, "Artificially soft and hard surfaces in electromagnetics," *IEEE Trans. Antennas Propagat.*, vol. 38, pp. 1537–1544, Oct. 1990.

[3] P. Pelet and N. Engheta, "The theory of chirowaveguides," *IEEE Trans. Antennas Propagat.*, vol. 38, pp. 90–97, Jan. 1990.

[4] N. Engheta and P. Pelet, "Mode orthogonality in chirowaveguides," *IEEE Trans. Microwave Theory Tech.*, vol. 38, pp. 1631–1634, Nov. 1990.

[5] S. F. Mahmoud, "Guided modes on open chirowaveguides," *IEEE Trans. Microwave Theory Tech.*, vol. 43, pp. 205–209, Jan. 1995.

[6] ——, "Mode characteristics in chirowaveguides with constant impedance walls," *J. Electromag. Waves Applicat.*, vol. 6, no. 5/6, pp. 625–640, 1992.

[7] I. V. Lindell, A. H. Sihvola, S. A. Tretyakov, and A. J. Viitanen, *Electromagnetic Waves in Chiral and Bi-Isotropic Media*. Norwood, MA: Artech House, 1994.

[8] F. Mariotte, S. A. Tretyakov, and B. Sauviac, "Isotropic chiral composite modeling: Comparison between analytical, numerical, and experimental results," *Microwave Opt. Technol. Lett.*, vol. 7, no. 18, pp. 861–864, 1994.

[9] R. E. Collin, *Foundations for Microwave Engineering*. New York: McGraw-Hill, 1966.